Chem Catalysis

CellPress

Article

Strong interaction-induced *in situ*-reconstructed Ag_3 triangle as a real active unit for enhanced electrocatalytic hydrogen evolution

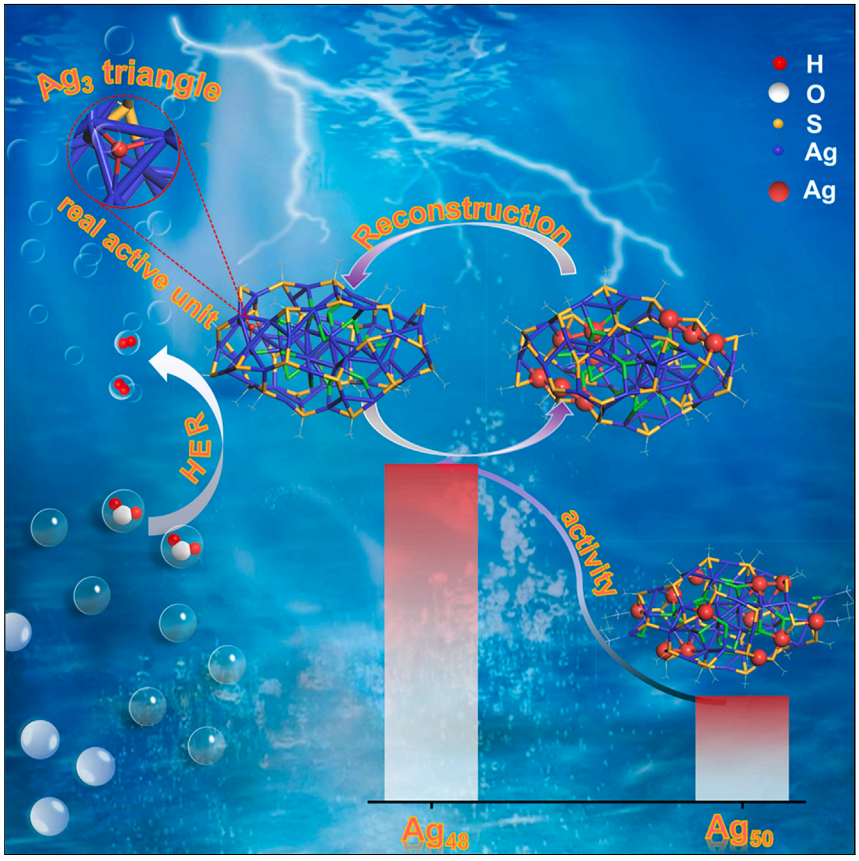

Ag_{48} and Ag_{50} have almost the same size and cluster framework, but Ag_{48} shows higher HER activity due to the *in situ*-reconstructed real active unit Ag_3 triangle. The stronger Ag-Ag interaction is the underlying reason for structural reconstruction. Based on this, two kinds of Ag_4 are designed to further confirm the strong interaction that induced the special Ag_3 triangle is the active unit for HER.

Yanting Zhou, Xiao Wei, Yuanxin Du, Kun Ni, Manzhou Zhu

duyuanxin@ahu.edu.cn (Y.D.)
nikun@ustc.edu.cn (K.N.)
zmz@ahu.edu.cn (M.Z.)

Highlights

Atomically precise metal nanocluster reveals the origin of structural reconstruction

In situ-reconstructed Ag_3 triangle unit is the real active unit for HER

The strong Ag-Ag interaction is the underlying reason for structural reconstruction

Zhou et al., Chem Catalysis 4, 101011
June 20, 2024
https://doi.org/10.1016/j.checat.2024.101011

Chem Catalysis

CellPress

Article

Strong interaction-induced *in situ*-reconstructed Ag_3 triangle as a real active unit for enhanced electrocatalytic hydrogen evolution

Yanting Zhou,[1] Xiao Wei,[1] Yuanxin Du,[1,*] Kun Ni,[2,*] and Manzhou Zhu[1,3,*]

SUMMARY

Due to the lack of well-defined structure, identifying and modulating structural reconstruction of a catalyst in reaction still remains a challenge. Herein, we prepared two atomically precise nanoclusters (Ag_{48} and Ag_{50}) with almost the same size and cluster framework. Ag_{48} showed higher electrocatalytic hydrogen evolution reaction (HER) activity than Ag_{50} due to an *in situ*-reconstructed real active unit Ag_3 triangle with appropriate hydrogen-binding energy. Based on *in situ* characterization and theoretical calculation, the structural reconstruction of Ag_{48} originated from the strong Ag-Ag interaction. Furthermore, two kinds of Ag_4 NCs were targeted for synthesis. The Ag_4 NC with stronger Ag-Ag interaction presented the Ag_3 triangle and exhibited better HER performance than the linear-type Ag_4 NC, validating the Ag_3 triangle arising from the strong interaction was the key for high HER activity. This study highlights the fundamental mechanism of interaction-induced structural reconstruction, providing useful guidelines for the design of a highly efficient catalyst.

INTRODUCTION

Accurate identification of the catalytic active site and an in-depth understanding of the catalytic mechanism are critical for the targeted design and practical application of highly efficient catalysts.[1–3] For a long time, it has been a consensus that catalysts exhibit steady configuration without structural transformation during the reaction.[4,5] With the development of *in situ* characterization techniques, structural reconstruction of catalysts inducing the formation of real active sites has been reported in recent years, especially in electrocatalytic reactions.[6–9] For example, lots of transition metal-based materials such as oxides,[10,11] sulfides,[12–14] phosphides,[15–17] layered double hydroxides,[18–20] and metal-organic frameworks,[21,22] etc., would undergo structure transformation under working conditions, preferring to derive to corresponding amorphous or low-crystalline metal oxyhydroxides and more reduced metallic-state species during electrooxidation and electroreduction process, respectively.[23–25] However, due to the complexity of the catalytic system under actual reaction conditions, and limited by the lack of model catalyst with precise composition and structure, deciphering the underlying origin of structural reconstruction is challenging.

Recently, atomically precise metal nanoclusters (NCs) have shown great potential in catalysis owing to their ultrasmall size, abundant uncoordinated active sites, and unique discrete electronic energy level.[26–30] More importantly, the precisely tunable composition, chemical environment, and configuration could further control the

THE BIGGER PICTURE

Accurate identification of the real catalytic sites is of great significance for targeted design of efficient catalysts and practical industrial application. For a long time, it has been agreed that the catalyst has a stable configuration during the reaction. Recently, benefiting from the development of *in situ* characterization techniques, more and more studies have found that synthesized catalysts may undergo structural reconstruction, in which the real catalytic active site is formed. However, due to the complexity of the catalytic system under work conditions and the lack of model catalysts with precise composition and structure, deciphering the origins of structural reconstruction is still a challenge. Herein, we utilize atomically precise metal nanoclusters with well-defined and controllable compositions and structures to reveal the underlying reason of interaction-induced structural reconstruction, providing useful guidelines for the design of a highly efficient catalyst.

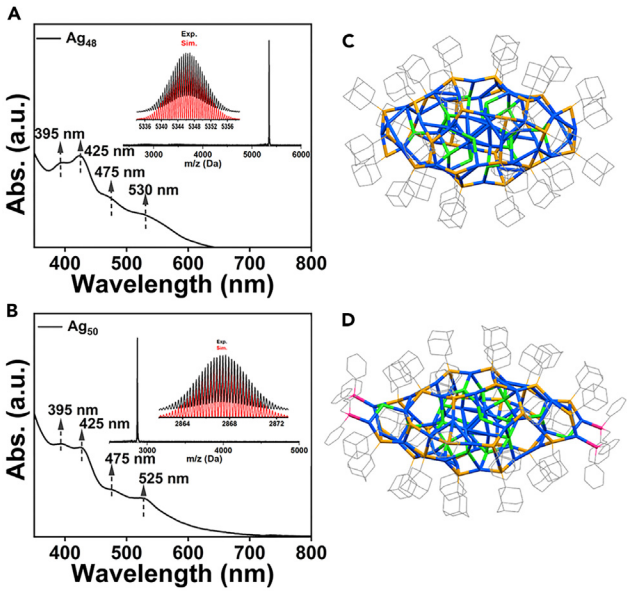

Figure 1. Structure and characterization of Ag_{48} and Ag_{50} NCs

(A and B) UV-vis absorption spectra of Ag_{48} and Ag_{50}, and the insets show the corresponding ESI-MS spectra.

(C and D) Overall crystal structure of Ag_{48} and Ag_{50}. Color codes: C = gray, Cl = green, Ag = blue, S = yellow, and P = magenta.

process and direction of structural reconstruction of catalyst during catalytic reaction, providing the opportunity for insight into the real active sites and catalytic mechanism at the atomic level.[31–37]

In this work, two Ag NCs (Ag_{48} and Ag_{50}) with almost the same size and cluster framework were synthesized and applied into electrocatalytic hydrogen evolution reaction (HER). Ag_{48} showed higher HER activity than Ag_{50} due to the *in situ*-reconstructed real active unit Ag_3 triangle, the center of which exhibited the appropriate binding energy of hydrogen. Thanks to the accurate structure, combined with *in situ* X-ray photoelectron spectroscopy (XPS) and theoretical calculation, the underlying reason for structural reconstruction was revealed, which is the stronger Ag-Ag interaction of Ag_{48} compared with Ag_{50}. Based on this, we designed and synthesized two kinds of Ag_4 NCs, and Ag_4 NCs with stronger Ag-Ag interaction displayed a triangular facet and showed better HER activity than the linear-type Ag_4 NCs, further confirming that the strong interaction that induced the special Ag_3 triangle was the active unit for HER.

RESULTS AND DISCUSSION

Structure and electrocatalytic HER performance of Ag_{48} and Ag_{50} NCs

Ag_{48} and Ag_{50} NCs (full name: $Ag_{48}Cl_{14}(S\text{-}Adm)_{30}$ and $Ag_{50}Cl_{16}(S\text{-}Adm)_{28}(DPPP)_2$, S-Adm = 1-adamantanethiolate, DPPP = 1,3-bis(diphenylphosphino)propane) were synthesized according to our previous work.[38] The measurements of electrospray ionization mass spectrometry (ESI-MS) and UV-vis absorption spectroscopy confirm the molecular purity of Ag_{48} and Ag_{50} (Figures 1A and 1B). The detailed construction diagrams of Ag_{48} and Ag_{50} NCs are shown in Figure S1. Both Ag_{48} and Ag_{50} NCs contain an identical Ag_8Cl_{14} kernel, which is composed of an octahedral Ag_6Cl_6 and two Ag_1Cl_4 units. The surfaces of the two NCs are based on the $Ag_{36}SR_{24}$ shell structure but are slightly different. Ag_{48} NCs contains an $Ag_{40}SR_{30}$ surface, while

[1]Department of Materials Science and Engineering, Centre for Atomic Engineering of Advanced Materials, Key Laboratory of Structure and Functional Regulation of Hybrid Materials of Ministry of Education, Key Laboratory of Functional Inorganic Material Chemistry of Anhui Province, Anhui University, Hefei 230601, China

[2]CAS Key Laboratory of Materials for Energy Conversion, Department of Materials Science and Engineering, iChEM, University of Science and Technology of China, Hefei, Anhui 230026 China

[3]Lead contact

*Correspondence: duyuanxin@ahu.edu.cn (Y.D.), nikun@ustc.edu.cn (K.N.), zmz@ahu.edu.cn (M.Z.)

https://doi.org/10.1016/j.checat.2024.101011

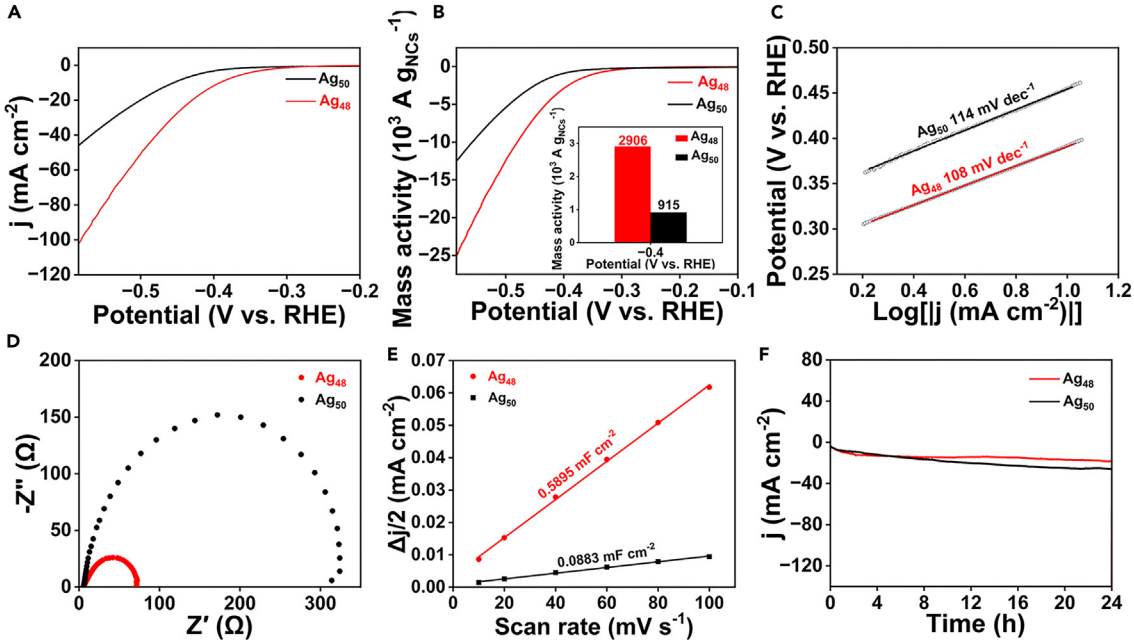

Figure 2. Electrocatalytic HER performance of Ag_{48} and Ag_{50} NCs

(A) HER polarization curves for Ag_{48} and Ag_{50}.

(B) Mass activities at various applied potentials of Ag_{48} and Ag_{50}. The inset shows the mass activity comparison at −0.4 V.

(C) Tafel plots of Ag_{48} and Ag_{50}.

(D) Impedance spectra of Ag_{48} and Ag_{50}.

(E) Determination of electrochemical double-layer capacitance by plotting capacitive currents with scanning rate.

(F) Chronopotentiometric curves at constant current density of 10 mA cm^{-2}.

Ag_{50} NCs possesses an $Ag_{42}SR_{28}Cl_2(L_3)_2$ surface. In addition, Ag_{50} NCs can be transformed from Ag_{48} NCs by adding two more AgL_3Cl but losing two SR. In addition, the atomic bond length on the surface shell of Ag_{48} and Ag_{50} NCs is similar, but the Ag coordination number is different. The Ag coordination number on the surface of Ag_{48} NCs is larger than that of Ag_{50} NCs (Table S1). Overall, the two NCs are highly correlated, with similar size and cluster framework, as shown in Figures 1C and 1D.

Routine electrochemical measurements were conducted to evaluate the HER activities of the two NCs. To assess the inherent activities of NCs, the NCs were deposited on chemically inert active carbon as working electrode, avoiding interference from other external factors. The two NCs were both isolated and uniformly dispersed on carbon support with a similar average size of ~1.46 nm (Figure S2). As can be seen from the linear sweep voltammetry (LSV) curves, Ag_{48} exhibits larger current density and lower onset overpotential than Ag_{50}. For achieving 10 mA cm^{-2} current density, Ag_{48} requires 392 mV overpotential, while Ag_{50} needs 455 mV (Figure 2A). As determined by inductively coupled plasma atomic emission spectrometry, the loading amounts of Ag_{48} and Ag_{50} are ~2 wt % and ~1.8 wt %, respectively (Table S2). The mass activity is further calculated by normalizing cluster mass to exclude the influence of loading amount.[39] Ag_{48} displays larger mass activity compared with Ag_{50}. At −0.4 V, the mass activity of Ag_{48} is 2,906 A g^{-1}, which is ~3.2-fold of Ag_{50} (915 A g^{-1}) (Figure 2B). The turnover frequency values of Ag_{48} and Ag_{50} NCs are 161.24 and 54.42 s^{-1} at −0.4 V, respectively. The LSV measurements of the HS-Adm and DPPP ligands and Ag-S-Adm and Ag-DPPP segments were also conducted to exclude the influence of ligand type. It can be seen that these ligands and segments are almost inactive for HER (Figures S3 and S4). The

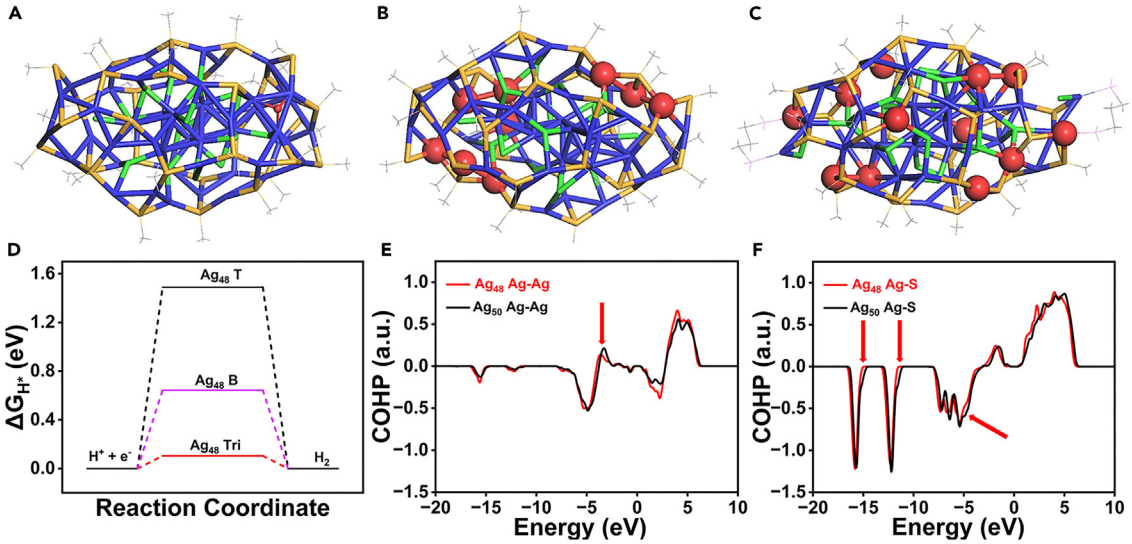

Figure 3. HER energetics and catalyst structure calculation

(A) Ag_{48} with H adsorbs on an Ag_3 triangular facet site. The red ball represents adsorbed H.

(B) The nine Ag atoms (marked by red balls) involved in forming three Ag_3 triangles in Ag_{48} during reconstruction.

(C) The corresponding Ag atom positions in Ag_{50}. Color codes: C = gray, Cl = green, Ag = blue, S = yellow, and P = magenta.

(D) Gibbs energy diagram of Ag_{48} for HER reaction.

(E) COHP analysis for Ag-Ag pairs in Ag_{48} and Ag_{50}.

(F) COHP analysis for Ag-S pairs in Ag_{48} and Ag_{50}. The red arrow in (E) and (F) guides the eye on the difference of the curves.

contact angles of the two NCs are similar and less than 90°, which excludes the influence of hydrophilic surfaces of the two NCs (Figure S5). The Tafel slope of Ag_{48} is 108 mV dec^{-1}, slightly lower than that of Ag_{50} (114 mV dec^{-1}) and close to 120 mV dec^{-1}, indicating that their rate-determining step is a Volmer step (Figure 2C). In addition, the electrochemical active surface areas (ECSAs) of Ag_{48} and Ag_{50} are estimated to be 2.89 and 0.43 cm^2, respectively. Ag_{48} shows larger ECSA and smaller electrochemical resistance (R_{ct}) compared with Ag_{50}, suggesting that Ag_{48} exhibits more active sites and faster charge transfer ability (Figures 2D, 2E, and S6). The stability of Ag_{48} was also tested as shown in Figure 2F. Ag_{50} NCs show a slight change in current density within the acceptable range, indicating the moderate long-term stability. Ag_{48} and Ag_{50} NCs remain monodispersed after the reaction, and the size is basically the same as before the reaction (Figure S7). All of the results demonstrate that Ag_{48} shows better electrocatalytic HER performance than Ag_{50}.

The exploration of the underlying reason for structural reconstruction

To figure out the reason for different HER activities, density functional theory (DFT) calculations were conducted. Interestingly, when Ag_{48} adsorbs H, its structure experiences spontaneous reconstruction. The most favorable adsorption site of H atom on Ag_{48} is the triangular facet site (Tri site), which corresponds to the adsorption of H on the center of an Ag_3 triangle, forming three H-Ag bonds, and shows the best HER activity with the ΔG_{H^*} of 0.1 eV (Figures 3A, 3D, and S8). The formation of an Ag_3 triangle during Ag_{48} reconstruction is detailed and shown in Video S1 in the supplemental information. The bridge site (B site), which corresponds to the adsorption of H on the middle of an Ag-Ag bond, forming two H-Ag bonds, shows a much lower HER activity than the Tri site (Figures 3D and S9). The top site (T site), which corresponds to the direct adsorption of H on an Ag atom, forming a single H-Ag bond, shows a sluggish HER activity (Figures 3D and S9). The ΔG_{H^*} shown in

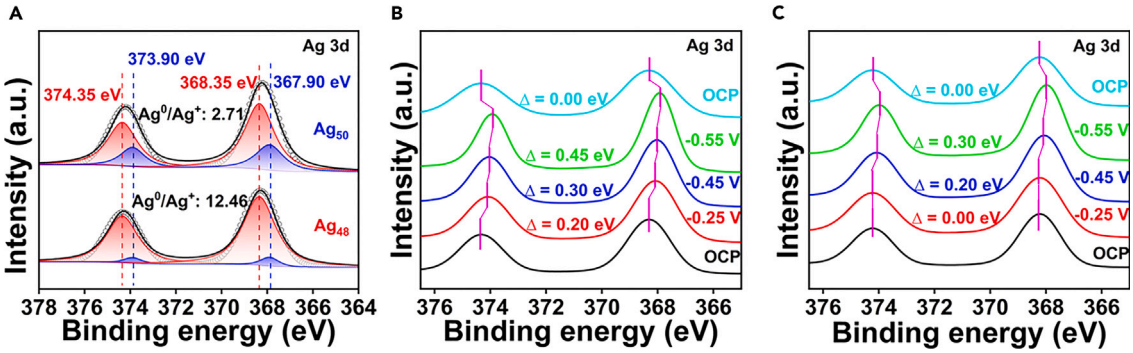

Figure 4. *In situ* XPS measurements

(A) The comparison of Ag XPS spectra of Ag_{48} and Ag_{50} before reaction.

(B and C) *In situ* Ag XPS spectra of Ag_{48} and Ag_{50}.

Figure 3D is the average value for each type of site. The ΔG_{H^*} values for all possible H adsorption sites of Ag_{48} NCs are shown in Figure S10 and Table S3.

During the reconstruction process, nine Ag atoms in Ag_{48} participate in the formation of three Ag_3 triangles (Figure 3B). Since the cluster framework of Ag_{48} and Ag_{50} is similar, we can label the corresponding Ag atom positions in Ag_{50}. Due to the symmetry of Ag_{50}, the corresponding twelve silver atoms are marked (Figure 3C). It is worth noting that these silver atoms in Ag_{50} are more dispersed, which is not conducive to the formation of a triangular facet. The ΔG_{H^*} data of these silver atoms in Ag_{50} NCs are provided in Table S4 and Figure S11. All the Ag atoms exhibit large ΔG_{H^*} values, which are not beneficial for HER. In addition, compared to Ag_{48}, Ag_{50} has two more Cl atoms, which are connected with two more Ag atoms located at both ends in Ag_{50} NCs. The ΔG_{H^*} values of the Ag atoms connected to the two more Cl atoms were also calculated, and their ΔG_{H^*} values are in the range from 0.55 to 1.68 eV, also indicating the poor HER activity (Figure S12; Table S5). Our DFT simulation results indicate that Ag_{48} experiences spontaneous structural reconstruction during the reaction, and the center of the *in situ*-formed Ag_3 triangular facet in Ag_{48} is the active site for HER.

The precise structure of the NC offers the opportunity for in-depth understanding of the origin of structural reconstruction. Crystal orbital Hamilton population (COHP) analysis reveals that the Ag-Ag bond in Ag_{48} is stronger than Ag_{50} due to the weaker anti-bonding state, as shown in Figure 3E. In addition, the Ag-S bond in Ag_{48} is weaker than Ag_{50} due to the weaker bonding state, as shown in Figure 3F. Based on the DFT analysis, the stronger Ag-Ag interaction but weaker Ag-S interaction could be the underlying reason for the structural transformation of Ag_{48}. In addition, the formation energies of Ag_{48} and Ag_{50} are −17.39 and −20.79 eV per cluster (see supplemental information for details), respectively, indicating that Ag_{48} is more unstable and prone to reconstruction than Ag_{50} (Table S6).

In situ XPS tests were measured to investigate the Ag-Ag interaction in the two NCs during HER process.[40–42] The peaks at 374.35 and 368.35 eV corresponded to Ag $3d_{3/2}$ and Ag $3d_{5/2}$ of Ag^0. The peaks located at 373.90 and 367.90 eV are assigned to Ag $3d_{3/2}$ and Ag $3d_{5/2}$ of Ag^+. The peak area ratio of Ag^0 and Ag^+ can be used as a reflection of their content ratio. Before reaction, the ratio of Ag^0 and Ag^+ in Ag_{48} is higher than that in Ag_{50}, indicating that Ag_{48} exhibits stronger Ag-Ag interaction (Figure 4A). Ag XPS spectra change with the increase of applied potential. It is worth noting that an obvious shift of Ag binding energy in Ag_{48} is observed when a

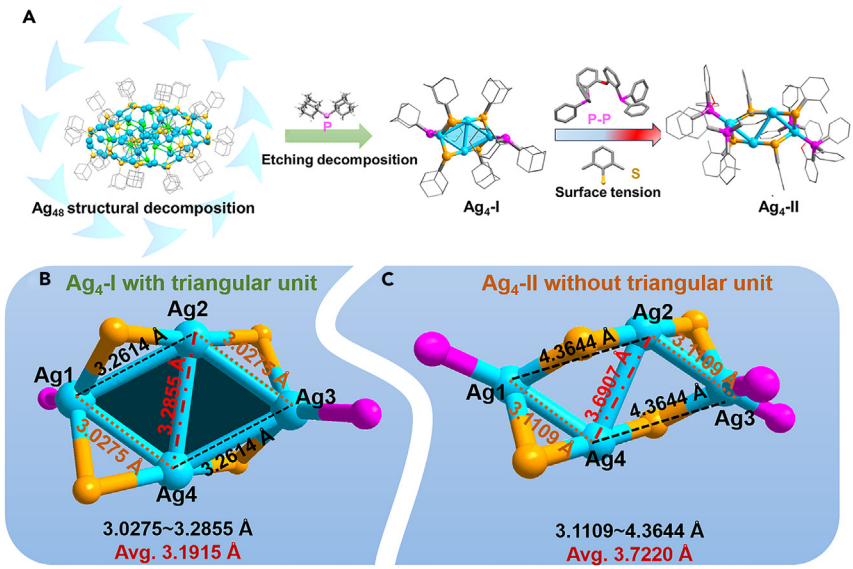

Figure 5. Synthesis and structural analysis of Ag_4-I and Ag_4-II

(A) Synthesis diagram of Ag_4-I and Ag_4-II.

(B and C) Structure comparison of Ag_4-I and Ag_4-II. Only sulfur atoms of thiolate ligands and the phosphorus atoms of the phosphine ligand are shown for clarity. Color codes: blue = Ag, yellow = S, and magenta = P.

potential of −0.25 V is applied, while the Ag XPS peak of Ag_{50} starts to change, requiring a higher potential of −0.45 V, suggesting Ag_{48} undergoes structural transformation at lower potential. Under the same potential of −0.55 V, the change of Ag binding energy in Ag_{48} is larger than that in Ag_{50}, demonstrating that the reconstruction degree of Ag_{48} is larger than Ag_{50} (Figures 4B and 4C). In addition, the Ag XPS spectra recover the same as before when the open circuit potential is applied again, indicating the structure transformation is reversible (Figures 4B and 4C).

Targeted synthesis of Ag_4 NCs with strong Ag-Ag interaction

On the basis of the above findings, two kinds of Ag_4 NCs with different Ag-Ag interaction strengths were targeted for synthesis to further verify the strong Ag-Ag interaction-induced Ag_3 triangle center is the key to achieve high-efficiency HER. The NC containing four Ag atoms is now available as the smallest structure to construct an Ag triangular and non-triangular unit in NCs with the same number of atoms. We used Ag_{48} NC as a template and introduced a large number of monodentate phosphine ligands to etch its structure, induced its decomposition and transformation, and finally obtained Ag_4-I NCs (Figure 5A). The Ag_4-I NC is composed of a double triangular unit of four Ag atoms that share an edge. The two Ag_3 units can be regarded as two isosceles triangles due to the similar Ag-Ag bond length (Figure 5B; Table S7). Ag_4-I NC was further transformed to linear-type Ag_4-II NC without a triangular unit by replacing HS-Adm with 2,6-dimethylbenzenethiol with relatively low steric hindrance (Figure 5A). As shown from the crystal structure, it is obvious that Ag-Ag interaction in Ag_4-I NC is stronger than that of Ag_4-II NC. Compared with Ag_4-I NC, the structure of Ag_4-II NC is stretched due to the existence of bidentate phosphine ligand, resulting in the distances of Ag1-Ag2 and Ag3-Ag4 getting longer and the triangular unit being broken (Figures 5B and 5C; Table S8).

The electrocatalytic HER activities of two Ag_4 NCs were evaluated. Ag_4-I shows a high current density of 88 mA cm^{-2} at −0.55 V and a low overpotential of 332 mV

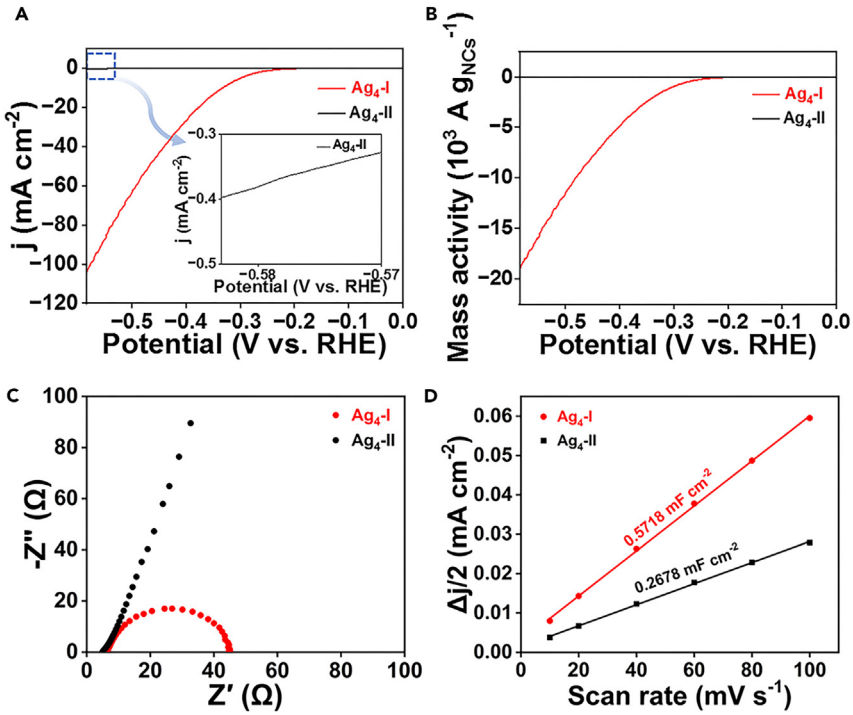

Figure 6. Evaluation of HER activity of Ag_4-I and Ag_4-II

(A) HER polarization curves for Ag_4-I and Ag_4-II. The inset shows an enlarged view of the dotted region.

(B) Mass activities of Ag_4-I and Ag_4-II.

(C) Electrochemical impedance spectra of Ag_4-I and Ag_4-II.

(D) Electrochemical double-layer capacitance of Ag_4-I and Ag_4-II.

for reaching 10 mA cm^{-2}, while the LSV curve of Ag_4-II is almost a flat line, suggesting that Ag_4-I exhibits high HER activity, and Ag_4-II has almost no activity for electrocatalytic HER (Figure 6A). Furthermore, Ag_4-I has higher mass activity, larger ECSAs, and more rapid electron transfer compared with Ag_4-II (Figures 6B–6D and S13). The HER performance of the ligands containing the two Ag_4 NCs was also tested, and they are almost inactive for HER; therefore, the difference in HER activities of the two Ag_4 NCs is attributed to the structural difference (Figure S14). In addition, DFT calculations further validate that the Ag_3 triangle center in Ag_4-I has better HER activity than Ag_4-II. The ΔG_{H^*} of HER for Ag_4-I is 0.43 eV and for Ag_4-II is −0.65 eV (Table S9). Thus, the Ag_3 triangle caused by strong Ag-Ag interaction in Ag_4-I NC is the real active unit for enhanced HER activity.

Conclusions

In summary, we synthesized Ag_{48} and Ag_{50} NCs and evaluated the HER performances. Ag_{48} displayed higher HER activity than Ag_{50}, which was attributed to the *in situ*-reconstructed Ag_3 triangle active unit. The center of the Ag_3 triangle showed a favorable binding ability of hydrogen. Benefiting from the precise structure, combined with *in situ* XPS and theoretical simulations, the fundamental mechanism of structural reconstruction of Ag_{48} was stronger Ag-Ag interaction compared with Ag_{50}. Based on the finding, Ag_4-I NCs with stronger Ag-Ag interaction showing an Ag_3 triangular facet were designed and synthesized, and they performed better than their counterpart (Ag_4-II NCs), further demonstrating the strong Ag-Ag interaction-induced Ag_3 triangle was crucial for high HER activity. This work

provides a thorough comprehension of strong interaction-induced structure evolution that will be helpful for designing a highly efficient catalyst with controlled reconstruction.

EXPERIMENTAL PROCEDURES

Resource availability

Lead contact

Further information and requests for resources should be directed to and will be fulfilled by the lead contact, Manzhou Zhu (zmz@ahu.edu.cn).

Materials availability

All materials generated in this study are available from the lead contact without restriction.

Data and code availability

All data needed to support the conclusions of this article are included in the main text or the supplemental information. CCDC numbers of Ag_4-I and Ag_4-II NC are 2329641 and 2329642, respectively.

Synthesis of Ag_{48} and Ag_{50}

Ag_{48} and Ag_{50} NCs (full name: $Ag_{48}Cl_{14}(S\text{-}Adm)_{30}$ and $Ag_{50}Cl_{16}(S\text{-}Adm)_{28}(DPPP)_2$) were synthesized based on one-pot reduction strategy according to our previous report.[34]

Synthesis of Ag_4-I

10 mg of Ag_{48} crystals was dissolved in 20 mL dichloromethane, 50 mg di-1-adamantylphosphine was added, and the reaction was stirred for 30 min. After that, the solution was rotavaporated under vacuum. The n-hexane/CH_2Cl_2 was used to wash/purify the synthesized NCs. The brownish-yellow crystal was obtained through internal diffusion method (dichloromethane: n-hexane = 1:3) in under 10 days.

Synthesis of Ag_4-II

10 mg of Ag_4-I crystals was dissolved in 20 mL dichloromethane, and 50 mg bis(2-diphenylphosphinophenyl)ether and 50 μL 2,6-dimethylbenzenethiol were added successively, and the reaction was stirred for 30 min. After that, the solution was rotavaporated under vacuum. The product purification method and single-crystal cultivation method were the same as for Ag_4-I.

SUPPLEMENTAL INFORMATION

Supplemental information can be found online at https://doi.org/10.1016/j.checat.2024.101011.

ACKNOWLEDGMENTS

We acknowledge the financial support of the Natural Science research project of Universities in Anhui Province (KJ2021ZD0001), Natural Science Foundation of Anhui Province (2208085MB20), and Natural Science Foundation of China (52273234, 52003265). The Supercomputing Center of USTC is acknowledged.

AUTHOR CONTRIBUTIONS

Y.Z. and X.W. contributed equally to this work. Y.Z. conducted the electrocatalytic experiments, performed the characterizations, and analyzed data. X.W. synthesized the clusters. Y.D. proposed and designed the experiments, wrote the paper, and

CellPress

managed the project. K.N. conducted the DFT simulation. Y.D., K.N., and M.Z. supervised the research and provided funding.

DECLARATION OF INTERESTS

The authors declare no competing interests.

Received: February 23, 2024
Revised: April 15, 2024
Accepted: May 7, 2024
Published: June 3, 2024

REFERENCES

1. Huang, L., Liu, Q., Wu, W., Gao, G., Zheng, X., Wang, J., and Dong, S. (2023). Identifying the active sites in unequal iron-nitrogen single-atom catalysts. Nat. Commun. *14*, 5594. https://doi.org/10.1038/s41467-023-41311-9.

2. Wang, W., Duan, J., Liu, Y., and Zhai, T. (2022). Structural Reconstruction of Catalysts in Electroreduction Reaction: Identifying, Understanding, and Manipulating. Adv. Mater. *34*, 2110699. https://doi.org/10.1002/adma.202110699.

3. Mao, J., Mei, B., Li, J., Yang, S., Sun, F., Lu, S., Chen, W., Song, F., and Jiang, Z. (2022). Unraveling the Dynamic Structural Evolution of Phthalocyanine Catalysts during CO_2 Electroreduction. Chin. J. Struct. Chem. *41*, 2210082–2210088. https://doi.org/10.14102/j.cnki.0254-5861.2022-0133.

4. Sun, H., Tung, C.-W., Qiu, Y., Zhang, W., Wang, Q., Li, Z., Tang, J., Chen, H.-C., Wang, C., and Chen, H.M. (2022). Atomic Metal–Support Interaction Enables Reconstruction-Free Dual-Site Electrocatalyst. J. Am. Chem. Soc. *144*, 1174–1186. https://doi.org/10.1021/jacs.1c08890.

5. Liu, X., Meng, J., Zhu, J., Huang, M., Wen, B., Guo, R., and Mai, L. (2021). Comprehensive Understandings into Complete Reconstruction of Precatalysts: Synthesis, Applications, and Characterizations. Adv. Mater. *33*, 2007344. https://doi.org/10.1002/adma.202007344.

6. Jin, Z., Li, P., Fang, Z., and Yu, G. (2022). Emerging Electrochemical Techniques for Probing Site Behavior in Single-Atom Electrocatalysts. Acc. Chem. Res. *55*, 759–769. https://doi.org/10.1021/acs.accounts.1c00785.

7. Timoshenko, J., and Roldan Cuenya, B. (2021). In Situ/Operando Electrocatalyst Characterization by X-ray Absorption Spectroscopy. Chem. Rev. *121*, 882–961. https://doi.org/10.1021/acs.chemrev.0c00396.

8. Chen, M., Liu, D., Qiao, L., Zhou, P., Feng, J., Ng, K.W., Liu, Q., Wang, S., and Pan, H. (2023). In-situ/operando Raman techniques for in-depth understanding on electrocatalysis. Chem. Eng. J. *461*, 141939. https://doi.org/10.1016/j.cej.2023.141939.

9. Jiang, Z. (2022). Preface to Advanced Characterization Technique in Electrocatalysis and Photocatalysis. Chin. J. Struct. Chem. *41*, 2210001. https://doi.org/10.14102/j.cnki.0254-5861.2022-0210.

10. He, L., Zhang, W., Mo, Q., Huang, W., Yang, L., and Gao, Q. (2020). Molybdenum Carbide-Oxide Heterostructures: In Situ Surface Reconfiguration toward Efficient Electrocatalytic Hydrogen Evolution. Angew. Chem. Int. Ed. *59*, 3544–3548. https://doi.org/10.1002/anie.201914752.

11. Zou, A., Tang, Y., Wu, C., Li, J., Meng, H., Wang, Z., Ma, Y., An, H., Zhong, H., Zhang, Q., et al. (2024). Understanding the Origin of Reconstruction in Transition Metal Oxide Oxygen Evolution Reaction Electrocatalysts. ChemSusChem *17*, e202301195. https://doi.org/10.1002/cssc.202301195.

12. Jiang, J., Zhang, Y.-J., Zhu, X.-J., Lu, S., Long, L.-L., and Chen, J.-J. (2021). Nanostructured metallic $FeNi_2S_4$ with reconstruction to generate FeNi-based oxide as a highly-efficient oxygen evolution electrocatalyst. Nano Energy *81*, 105619. https://doi.org/10.1016/j.nanoen.2020.105619.

13. Zhao, C.-X., Liu, J.-N., Wang, C., Wang, J., Song, L., Li, B.-Q., and Zhang, Q. (2022). An anionic regulation mechanism for the structural reconstruction of sulfide electrocatalysts under oxygen evolution conditions. Energy Environ. Sci. *15*, 3257–3264. https://doi.org/10.1039/D2EE01036D.

14. Nguyen, T.X., Su, Y.-H., Lin, C.-C., and Ting, J.-M. (2021). Self-Reconstruction of Sulfate-Containing High Entropy Sulfide for Exceptionally High-Performance Oxygen Evolution Reaction Electrocatalyst. Adv. Funct. Mater. *31*, 2106229. https://doi.org/10.1002/adfm.202106229.

15. Zhao, Y., Dongfang, N., Triana, C.A., Huang, C., Erni, R., Wan, W., Li, J., Stoian, D., Pan, L., Zhang, P., et al. (2022). Dynamics and control of active sites in hierarchically nanostructured cobalt phosphide/chalcogenide-based electrocatalysts for water splitting. Energy Environ. Sci. *15*, 727–739. https://doi.org/10.1039/D1EE02249K.

16. Chu, H., Feng, P., Jin, B., Ye, G., Cui, S., Zheng, M., Zhang, G.-X., and Yang, M. (2022). In-situ release of phosphorus combined with rapid surface reconstruction for Co-Ni bimetallic phosphides boosting efficient overall water splitting. Chem. Eng. J. *433*, 133523. https://doi.org/10.1016/j.cej.2021.133523.

17. Zhang, Y., Lee, S., Jeong, S., Son, E., Baik, J.M., Han, Y.-K., and Park, H. (2024). Phase-Bridged Hierarchical Catalysts for Efficient and Stable Water Electrolysis. Adv. Funct. Mater. *34*, 2309250. https://doi.org/10.1002/adfm.202309250.

18. Lei, H., Ma, L., Wan, Q., Tan, S., Yang, B., Wang, Z., Mai, W., and Fan, H.J. (2022). Promoting Surface Reconstruction of NiFe Layered Double Hydroxide for Enhanced Oxygen Evolution. Adv. Energy Mater. *12*, 2202522. https://doi.org/10.1002/aenm.202202522.

19. Enkhtuvshin, E., Yeo, S., Choi, H., Kim, K.M., An, B.-S., Biswas, S., Lee, Y., Nayak, A.K., Jang, J.U., Na, K.-H., et al. (2023). Surface Reconstruction of Ni-Fe Layered Double Hydroxide Inducing Chloride Ion Blocking Materials for Outstanding Overall Seawater Splitting. Adv. Funct. Mater. *33*, 2214069. https://doi.org/10.1002/adfm.202214069.

20. Hua, W., Sun, H., Ren, L., Li, Y., and Wang, J.-G. (2021). 2-Methylimidazole-induced reconstruction of cobalt (oxy)hydroxide electrocatalysts toward efficient water oxidation. Chem. Eng. J. *420*, 129717. https://doi.org/10.1016/j.cej.2021.129717.

21. Zhang, C., Qi, Q., Mei, Y., Hu, J., Sun, M., Zhang, Y., Huang, B., Zhang, L., and Yang, S. (2023). Rationally Reconstructed Metal-Organic Frameworks as Robust Oxygen Evolution Electrocatalysts. Adv. Mater. *35*, 2208904. https://doi.org/10.1002/adma.202208904.

22. Lin, X., Li, X., Shi, L., Ye, F., Liu, F., and Liu, D. (2023). In Situ Electrochemical Restructuring B-Doped Metal-Organic Frameworks as Efficient OER Electrocatalysts for Stable Anion Exchange Membrane Water Electrolysis. Small, e2308517. First published: 28 December 2023. https://doi.org/10.1002/smll.202308517.

23. Zhong, H., Zhang, Q., Yu, J., Zhang, X., Wu, C., Ma, Y., An, H., Wang, H., Zhang, J., Wang, X., and Xue, J. (2023). Fundamental Understanding of Structural Reconstruction Behaviors in Oxygen Evolution Reaction Electrocatalysts. Adv. Energy Mater. *13*, 2301391. https://doi.org/10.1002/aenm.202301391.

24. Wang, J. (2023). Controlling dynamic reconstruction chemistry for superior oxygen-evolving catalysts. Chem *9*, 1645–1657. https://doi.org/10.1016/j.chempr.2023.06.001.

25. Cao, L., Liu, Y., Xu, C., Zhou, Z., Zhao, P., Niu, S., Huang, Q., Wu, Y., Yang, J., Yao, T., et al. (2019). Identification of single-atom active sites in carbon-based cobalt catalysts during electrocatalytic hydrogen evolution. Nat.

Catal. *102*, 134–141. https://doi.org/10.1038/s41929-018-0203-5.

26. Liu, Y., Yu, J., Lun, Y., Wang, Y., Wang, Y., and Song, S. (2023). Ligand Design in Atomically Precise Copper Nanoclusters and Their Application in Electrocatalytic Reactions. Adv. Funct. Mater. *33*, 2304184. https://doi.org/10.1002/adfm.202304184.

27. Liu, X., Cai, X., and Zhu, Y. (2023). Catalysis Synergism by Atomically Precise Bimetallic Nanoclusters Doped with Heteroatoms. Acc. Chem. Res. *56*, 1528–1538. https://doi.org/10.1021/acs.accounts.3c00118.

28. Yan, J., Teo, B.K., and Zheng, N. (2018). Surface Chemistry of Atomically Precise Coinage–Metal Nanoclusters: From Structural Control to Surface Reactivity and Catalysis. Acc. Chem. Res. *51*, 3084–3093. https://doi.org/10.1021/acs.accounts.8b00371.

29. Hu, J., Zhou, M., Li, K., Yao, A., Wang, Y., Zhu, Q., Zhou, Y., Huang, L., Pei, Y., Du, Y., et al. (2023). Evolution of Electrocatalytic CO_2 Reduction Activity Induced by Charge Segregation in Atomically Precise AuAg Nanoclusters Based on Icosahedral M_{13} Unit 3D Assembly. Small *19*, 2301357. https://doi.org/10.1002/smll.202301357.

30. Qin, L., Ma, G., Wang, L., and Tang, Z. (2021). Atomically precise metal nanoclusters for (photo)electroreduction of CO_2: Recent advances, challenges and opportunities. J. Energy Chem. *57*, 359–370. https://doi.org/10.1016/j.jechem.2020.09.003.

31. Wu, Q.-J., Si, D.-H., Sun, P.-P., Dong, Y.-L., Zheng, S., Chen, Q., Ye, S.-H., Sun, D., Cao, R., and Huang, Y.-B. (2023). Atomically Precise Copper Nanoclusters for Highly Efficient Electroreduction of CO_2 towards Hydrocarbons via Breaking the Coordination Symmetry of Cu Site. Angew. Chem. Int. Ed. *62*, e202306822. https://doi.org/10.1002/anie.202306822.

32. Liu, L., Zheng, S.-J., Chen, H., Cai, J., and Zang, S.-Q. (2024). Tandem Nitrate-to-Ammonia Conversion on Atomically Precise Silver Nanocluster/MXene Electrocatalyst. Angew. Chem. Int. Ed. *63*, e202316910. https://doi.org/10.1002/anie.202316910.

33. Li, Y., Li, S., Nagarajan, A.V., Liu, Z., Nevins, S., Song, Y., Mpourmpakis, G., and Jin, R. (2021). Hydrogen Evolution Electrocatalyst Design: Turning Inert Gold into Active Catalyst by Atomically Precise Nanochemistry. J. Am. Chem. Soc. *143*, 11102–11108. https://doi.org/10.1021/jacs.1c04606.

34. Yuan, S.-F., Lei, Z., Guan, Z.-J., and Wang, Q.-M. (2021). Atomically Precise Preorganization of Open Metal Sites on Gold Nanoclusters with High Catalytic Performance. Angew. Chem. Int. Ed. *60*, 5225–5229. https://doi.org/10.1002/anie.202012499.

35. Zhuang, S., Chen, D., Fan, W., Yuan, J., Liao, L., Zhao, Y., Li, J., Deng, H., Yang, J., Yang, J., and Wu, Z. (2022). Single-Atom-Kernelled Nanocluster Catalyst. Nano Lett. *22*, 7144–7150. https://doi.org/10.1021/acs.nanolett.2c02290.

36. Seong, H., Efremov, V., Park, G., Kim, H., Yoo, J.S., and Lee, D. (2021). Atomically Precise Gold Nanoclusters as Model Catalysts for Identifying Active Sites for Electroreduction of CO_2. Angew. Chem. Int. Ed. *60*, 14563–14570. https://doi.org/10.1002/anie.202102887.

37. Qin, L., Sun, F., Ma, X., Ma, G., Tang, Y., Wang, L., Tang, Q., Jin, R., and Tang, Z. (2021). Homoleptic Alkynyl-Protected Ag_{15} Nanocluster with Atomic Precision: Structural Analysis and Electrocatalytic Performance toward CO_2 Reduction. Angew. Chem. Int. Ed. *60*, 26136–26141. https://doi.org/10.1002/anie.202110330.

38. Wei, X., Shen, H., Xu, C., Li, H., Jin, S., Kang, X., and Zhu, M. (2021). Ag_{48} and Ag_{50} Nanoclusters: Toward Active-Site Tailoring of Nanocluster Surface Structures. Inorg. Chem. *60*, 5931–5936. https://doi.org/10.1021/acs.inorgchem.1c00355.

39. Cheng, X., Li, Y., Zheng, L., Yan, Y., Zhang, Y., Chen, G., Sun, S., and Zhang, J. (2017). Highly active, stable oxidized platinum clusters as electrocatalysts for the hydrogen evolution reaction. Energy Environ. Sci. *10*, 2450–2458. https://doi.org/10.1039/C7EE02537H.

40. He, Y., Liu, S., Wang, M., Cheng, Q., Ji, H., Qian, T., and Yan, C. (2023). Advanced In Situ Characterization Techniques for Direct Observation of Gas-Involved Electrochemical Reactions. Energy Environ. Mater. *6*, e12552. https://doi.org/10.1002/eem2.12552.

41. Xu, W., Wang, Z., Liu, P., Tang, X., Zhang, S., Chen, H., Yang, Q., Chen, X., Tian, Z., Dai, S., et al. (2024). Ag Nanoparticle-Induced Surface Chloride Immobilization Strategy Enables Stable Seawater Electrolysis. Adv. Mater. *36*, 2306062. https://doi.org/10.1002/adma.202306062.

42. Yun, H., Choi, W., Shin, D., Oh, H.-S., and Hwang, Y.J. (2023). Atomic Arrangement of AuAg Alloy on Carbon Support Enhances Electrochemical CO_2 Reduction in Membrane Electrode Assembly. ACS Catal. *13*, 9302–9312. https://doi.org/10.1021/acscatal.3c01044.